Geophysical Journal International

Geophys. J. Int. (2017) **211,** 1640–1654
Advance Access publication 2017 September 21
GJI Seismology

doi: 10.1093/gji/ggx388

Linking source region and ocean wave parameters with the observed primary microseismic noise

C. Juretzek[1,2] and C. Hadziioannou[1,2]

[1]*Department of Earth and Environmental Sciences, LMU, D-*80333 *Munich, Germany. E-mail: carina.juretzek@googlemail.com*
[2]*Institute of Geophysics, Center for Earth System Research and Sustainability (CEN), Universität Hamburg, D-*20146 *Hamburg, Germany*

Accepted 2017 September 20. Received 2017 September 6; in original form 2017 January 27

SUMMARY

In previous studies, the contribution of Love waves to the primary microseismic noise field was found to be comparable to those of Rayleigh waves. However, so far only few studies analysed both wave types present in this microseismic noise band, which is known to be generated in shallow water and the theoretical understanding has mainly evolved for Rayleigh waves only. Here, we study the relevance of different source region parameters on the observed primary microseismic noise levels of Love and Rayleigh waves simultaneously. By means of beamforming and correlation of seismic noise amplitudes with ocean wave heights in the period band between 12 and 15 s, we analysed how source areas of both wave types compare with each other around Europe. The generation effectivity in different source regions was compared to ocean wave heights, peak ocean gravity wave propagation direction and bathymetry. Observed Love wave noise amplitudes correlate comparably well with near coastal ocean wave parameters as Rayleigh waves. Some coastal regions serve as especially effective sources for one or the other wave type. These coincide not only with locations of high wave heights but also with complex bathymetry. Further, Rayleigh and Love wave noise amplitudes seem to depend equally on the local ocean wave heights, which is an indication for a coupled variation with swell height during the generation of both wave types. However, the wave-type ratio varies directionally. This observation likely hints towards a spatially varying importance of different source mechanisms or structural influences. Further, the wave-type ratio is modulated depending on peak ocean wave propagation directions which could indicate a variation of different source mechanism strengths but also hints towards an imprint of an effective source radiation pattern. This emphasizes that the inclusion of both wave types may provide more constraints for the understanding of acting generation mechanisms.

Key words: Europe; Time-series analysis; Seismic noise; Surface waves and free oscillations.

1 INTRODUCTION

Primary microseismic noise is known to be generated in shallow water by linear coupling of ocean gravity wave energy into seismic wave energy at the same period (Haubrich & McCamy 1969). Due to this direct coupling, noise levels are known to correlate well with ocean wave heights at nearby shores (e.g. Bromirski 2001; Barruol *et al.* 2006) and are affected by the presence of sea-ice (Stutzmann *et al.* 2009) and tidal sea-level variations in the shallow coast regions (Young *et al.* 2013; Beucler *et al.* 2015). Various authors investigated the possibilities to deduce short term local swell heights as well as long term variations of climate related ocean wave weather from seismic noise amplitudes (e.g. Bromirski *et al.* 1999; Grevemeyer *et al.* 2000; Aster *et al.* 2008; Ebeling 2012; Ferretti *et al.* 2013). Recently, Ardhuin *et al.* (2015) made a detailed quantitative estimate of seismic noise levels due to pressure variations generated by ocean gravity waves propagating in shallow water in the presence of seafloor slopes, as proposed by Hasselmann (1963). They found a good agreement between theoretical expectations and measurements of vertical component noise levels due to this mechanism in the primary microseismic and the hum frequency bands.

A theoretical framework has mainly evolved for Rayleigh waves only. However, in previous studies, the contribution of Love waves to the primary microseismic noise field was found to be comparable to or even larger than those of Rayleigh waves (e.g. Friedrich *et al.* 1998; Lin *et al.* 2008; Nishida *et al.* 2008). Observations of the primary microseimic noise field showed that both wave types are generally observed from similar directions but with different azimuthal amplitude distributions at a variety of geographic locations (Behr *et al.* 2013; Poli *et al.* 2013; Juretzek & Hadziioannou 2016). This poses the question whether the directional wave type ratio variations arise due to structural influence along the propagation path or emerge in the source region. Since crustal heterogeneities become increasingly important for surface wave propagation

© The Authors 2017. Published by Oxford University Press on behalf of The Royal Astronomical Society.

Downloaded from https://academic.oup.com/gji/article-abstract/211/3/1640/4209579
by Staats- und Universitätsbibliothek Hamburg user
on 19 December 2017

towards higher frequencies, wave type conversions at, for example, continental margins (Gregersen 1978) or along the propagation path (Kennett & Mykkeltveit 1984), and scattering of Rayleigh waves at structural features with length scales of the order of the surface wave wavelength (e.g. Kennett 1972) could be a possible explanation for the presence of Love waves in the microseimic noise bands. However, suggestions how Rayleigh and Love waves could be excited simultaneously by source mechanisms were made by Friedrich *et al.* (1998) and Fukao *et al.* (2010). While the theoretical frameworks by Hasselmann (1963) and Fukao *et al.* (2010) focus on sources with effective isotropic seismic wave radiation, Saito (2010) and Friedrich *et al.* (1998) described how the presence of bathymetry structure could cause directive sources with different effective radiation patterns for both wave types, which can be dependent on ocean gravity wave propagation direction.

For the purpose of understanding the relevance of different parameters on the observed surface wave noise levels, we test the influence of different earth and ocean properties in the source region on the Love and Rayleigh wave noise strength. In this study we

(i) resolve primary microseismic source areas of Love waves in comparison to Rayleigh waves by correlating seismic noise with ocean surface elevation and by array based localizations,

(ii) measure the relation between ocean wave height and seismic noise amplitude of both wave types as a measure of noise generation effectivity at different locations,

(iii) compare the relative Love and Rayleigh wave noise generation effectivity in different source regions with different parameters such as ocean surface elevation, ocean gravity wave propagation direction and bathymetry.

2 DATA AND SEISMIC OBSERVATIONS OF PRIMARY MICROSEISMIC NOISE

In order to investigate azimuthal variation in primary microseimic noise strength of both wave types, and to resolve source regions of Love and Rayleigh waves by noise observations at multiple locations, we use seismic array data and apply a frequency domain three-component Capon beamforming based on Esmersoy *et al.* (1985) and explained by Riahi *et al.* (2013) in more detail. Here, we analyse noise signals on vertical, radial and transversal components. Our data set includes publicly available three-component seismic data of permanent stations from the Norwegian Seismic Array (NOA), and from selected stations CH of the Swiss Seismological Service (SED; https://doi.org/10.12686/sed/networks/ch) over a time span of a full year in 2013 to capture effects of seasonal variations in noise generation. Additionally, we use data for the period from 2008 December 1 to 2009 February 28 from the temporary LAPNET/POLNET array (Kozlovskaya 2007), in order to enhance the available azimuthal range of our observation locations with respect to the noise sources. From studies analysing seismic noise properties during periods of several years, (e.g. Schimmel *et al.* 2011), we know that the average properties of microseismic noise are similar for the same season over different years. Therefore, we add this data set for a comparison between dominant source regions during, for example, Northern Hemisphere winter, when strong primary microseismic noise is generated in Northern Hemisphere oceans around Europe (e.g. Stutzmann *et al.* 2009). Since there were many stations and the array covered a large area, we are able to divide the network into a northern and central sub-array, LAPN and LAPM respectively.

Using Obspy 1.0.2. (The ObsPy Development Team 2016) we apply standard processing steps, consisting of demeaning, linear detrending, bandpass filtering (4th order Butterworth-Bandpass 0.04–0.25 Hz), resampling (1 Hz) and deconvolving the instrument response from the seismic data. The data was divided into windows of 512 s length with 50 per cent overlap, and tapered with a Tukey window. We removed each time window which was dominated by highly energetic transients in the frequency range between 0.05 and 0.1 Hz, by defining a STA/LTA variance ratio rejection threshold of 2 with a long-term average of one day. The cross-covariance matrix of the Fourier transformed velocity seismograms is temporally averaged over 42 windows giving intervals of approximately 3 hr, which equals the sampling rate of the ocean wave parameter data used in this study. The number of data snapshots that form the average of the cross-covariance matrix was large enough to obtain stable Capon beamforming solutions for the array configurations used.

For the purpose of gaining insight into primary microseimic Love wave generation, we want to analyse how source directions of the highest average noise amplitudes of Love and Rayleigh waves compare with each other, and how they relate to specific source regions. In Europe, long periodic primary microseimic noise (e.g. periods $\geq$20 s) can be observed from large distances (e.g. Yang Ritzwoller 2008; Matsuzawa *et al.* 2012; Sadeghisorkhani *et al.* 2016). Therefore, we restrict our analysis to the primary microseismic peak range (12–15 s), where the influence of attenuation suppresses very distant source regions.

We additionally use the phase velocity as selection criterion between the two wave types. Phase velocities of fundamental mode Love and Rayleigh waves at the array sites were determined in a previous study (Juretzek & Hadziioannou 2016). We consider vertical, radial, and transversal component beamformer results and form the mean of each component over the total time span analysed.

Fig. 1(a) shows slowness versus backazimuth plots of the self-normalized mean beampower on the transversal component and the sum of the mean vertical and radial component results. The typically observed slowness range of signals on the different components is highlighted by white solid lines and agrees with our two target wave types. Love waves (transversal beamformer result) and Rayleigh waves (vertical+radial beamformer results) share similar backazimuth ranges corresponding to local beampower peaks. However, we observe primarily different source directions for the noise amplitude maxima between the wave types. This characteristic holds for window lengths between 128–512 s and covariance matrix averaging lengths between 1.5–3 hr as inferred from additional tests. Since the azimuthal noise distributions of the individual radial and vertical component results were found to be very similar, azimuthal ellipticity differences of Rayleigh waves do not seem to cause these differences. Primary microseimic wave type differences with azimuth were previously observed at different locations (Behr *et al.* 2013; Juretzek & Hadziioannou 2016). Although inhomogeneous structures beneath the array could cause such effects, the consistency between observations likely hints to common source or propagation path effects.

Pronounced seasonal variations in noise strength are a well-known feature at mid and high latitudes (Stutzmann *et al.* 2009), and results in Fig. 1(a) are likely dominated by the winter results. Since we are also interested in the most common azimuthal noise amplitude distribution at the arrays in this study we self-normalized each 3 hourly slowness versus backazimuth beamform result and take their median over the total time span analysed. For an illumination of the geographic regions which correspond to high relative beampower, the maximum amplitudes within the highlighted

Downloaded from https://academic.oup.com/gji/article-abstract/211/3/1640/4209579
by Staats- und Universitätsbibliothek Hamburg user
on 19 December 2017

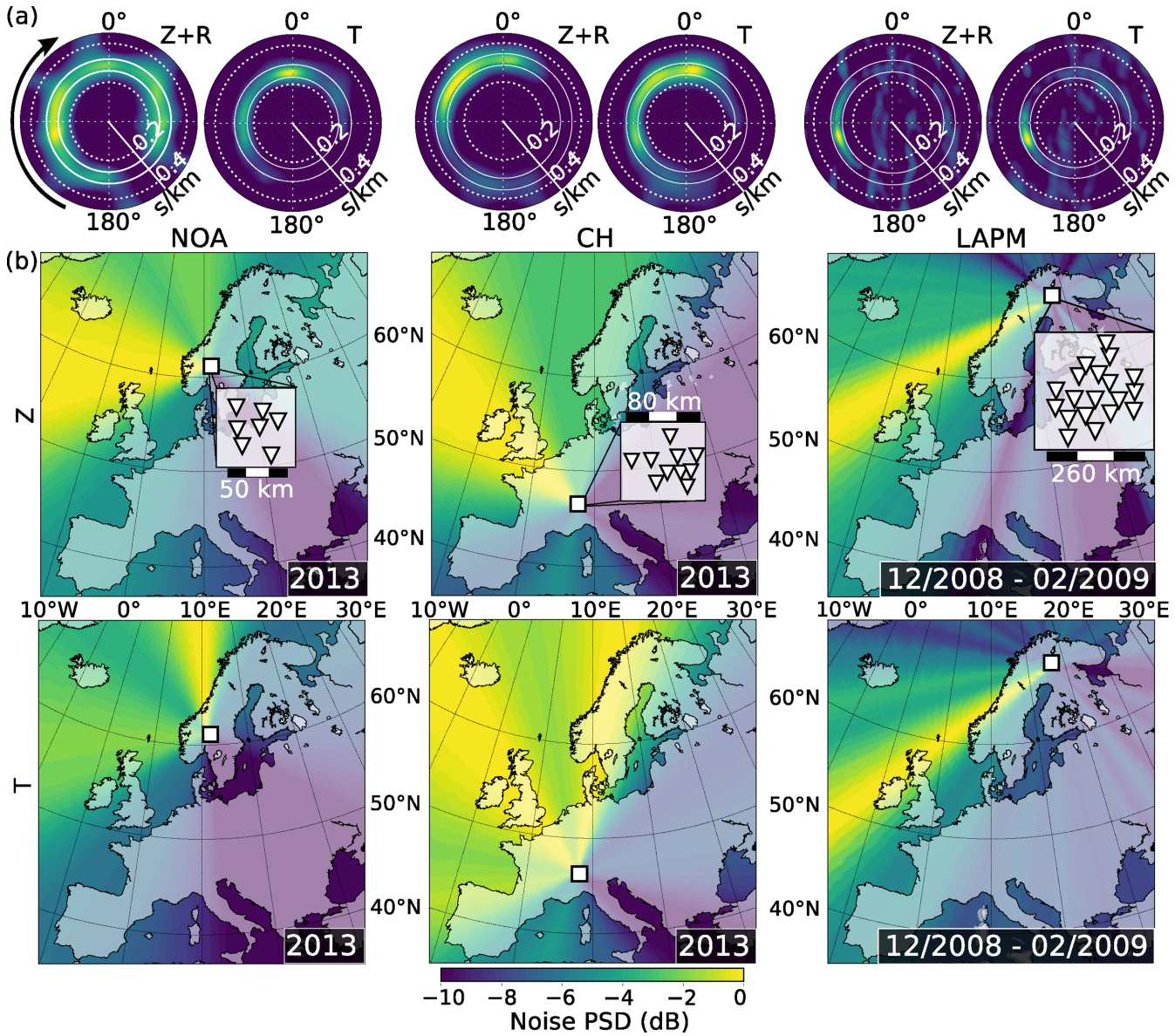

Figure 1. Self-normalized mean beampower PSD for vertical (Z), radial (R) and transversal (T) component noise observations in slowness versus backazimuth representation (a), and self-normalized median beampower PSD as backprojection from the array centres according to great circle path propagation (b) at three different array sites (white squares show station geometry) and a period of 15.1 s. Labels in maps indicate the time span of the data averages for (a) and (b) and the same colour scale is used for (a) and (b). The arrow indicates the backazimuth clockwise from North.

slowness range in Fig. 1(a), is back-projected for each array according to great circle path propagation as shown in Fig. 1(b).

We constantly find an illumination of the western coasts of Norway and the British Isles, which agrees with other publications (e.g. Friedrich *et al.* 1998; Kimman *et al.* 2012; Möllhoff & Bean 2016; Sadeghisorkhani *et al.* 2016). Since simultaneous signals from similar directions of arrival below the resolution limits of an array cause distorted beampower and signal parameters as addressed by Gal *et al.* (2016), caution must be taken in the interpretation of results. The arrays used here, have different resolution capabilities, and azimuthal distributions with respect to the source areas. Still, wave type amplitude differences agree between the arrays, which indicates a sufficient resolution for the regional source areas.

For a better understanding of the time dependence of directional amplitude differences between the wave types found in Figs 1(a) and (b), we form daily means for beampower at the Norsar array and for corresponding wave heights near the Norwegian shore. Fig. 2 shows these means for few days in December 2013. Although the beampower pattern of both wave types resemble each other, maximum Rayleigh wave amplitudes tend to follow the highest wave height locations. Love wave amplitudes from specific northern backazimuths remain on a higher level in addition to weaker varying amplitude maxima, which follow largest ocean wave heights. Azimuthal strength differences that were observed for the yearly results (Fig. 1) are reflected in these daily averages. This relatively stronger transversal component beampower peak indicates significant horizontally polarized ground motions that occur even for moderate near coastal wave heights north of the array, as estimated from WAVEWATCH III® modelled ocean wave parameters. Ocean wave model resources are described in more detail in Section 4. Such deviations between differently polarized seismic signals could likely arise due

Downloaded from https://academic.oup.com/gji/article-abstract/211/3/1640/4209579
by Staats- und Universitätsbibliothek Hamburg user
on 19 December 2017

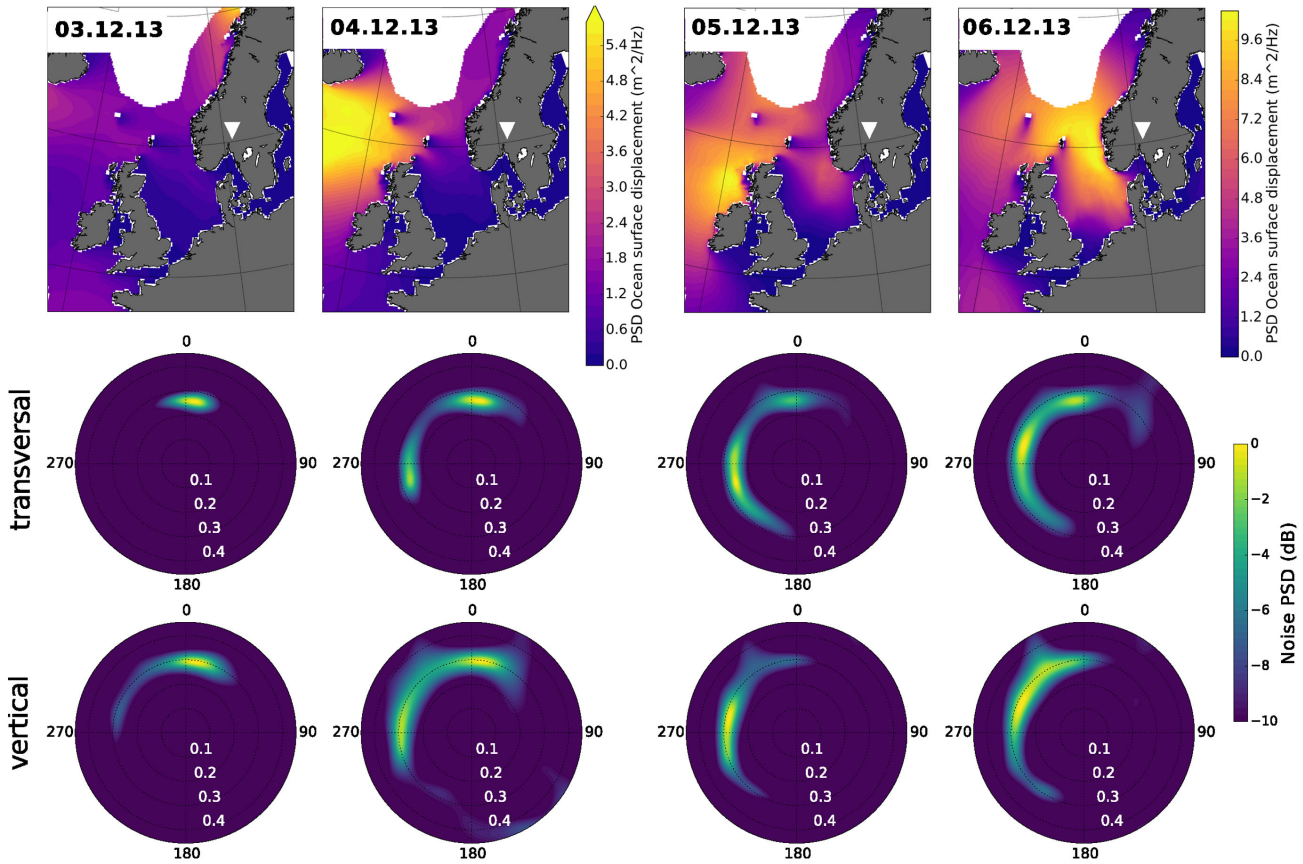

Figure 2. Sequence of 4 days in December 2013, showing daily averages of ocean wave height (top) and of vertical and transversal beampower spectral density as backazimuth versus slowness diagrams (bottom) for the Norsar array (triangle indicates array centre).

to locally different source processes and propagation effects in heterogeneous earth structure.

3 STRUCTURAL EFFECTS

It is well known that crustal heterogeneities cause substantial refraction of surface waves at the microseimic period range and at longer periods (e.g. Oliver 1962). Cotte *et al.* (2000) found up to 30° of azimuthal deviations for Rayleigh and Love waves at periods above 20 s in the French Alps. In a different study Paulssen *et al.* (1990) observed strong surface wave amplitude distortions and great circle path deviations in southern Spain for Rayleigh waves from teleseismic events and suggest scattering, defocusing and anelastic attenuation as possible causes. This is an obstacle for the process of source localization approaches, which rely on back-projection as applied in this study, especially when observing signals from far-field distances.

Especially for the central European Swiss array (CH), great circle path deviations are likely not negligible, since wave propagation distances across complex structure are considerably large in this case. With focus on this array, we choose two approaches to obtain a best estimate of the structural influence on the surface wave propagation from the source. We measure travel path deviations using a number of earthquakes mainly located near typical noise source regions on one hand, and we use ray tracing in a regional velocity model on the other.

In a first approach, we compare theoretical backazimuths of surface wave arrivals for a number of regional earthquakes, detailed in Supporting Information Table S1, to their backazimuths observed with beamforming at the Swiss array.

In a second approach, we test whether a seismic velocity model for the European region is able to reproduce observed travel path deviations at our frequency range of interest. We use the velocity model described in Afanasiev *et al.* (2016), which was derived from a combination of available velocity models of multiple scales and therefore includes regional information wherever possible. Processing details for both approaches and a comparison between results from both approaches are detailed in the Supporting Information. We conclude, that this velocity model is suitable to serve as an indicator of the propagation deviation strength.

Fig. 3 shows the earthquake derived great circle path deviations (labels) and direction dependent travel path deviations, estimated by ray tracing into different propagation directions from three array centres (lines). The estimated deviations to great circle path backazimuth are mainly within a range of few degrees in the distance range and azimuthal range of strong primary microseismic noise sources. However, deviations for surface waves propagating from the southwestern most coasts of Europe are larger, which could be related to a lack of significant surface wave amplitudes from these azimuths. In most cases, backazimuths for Rayleigh waves deviate more strongly from the great circle path assumption than for Love waves. Those deviations could explain moderate differences between Rayleigh and Love wave beamformer peak azimuths, for example, observed at CH for the British Isles direction (*cf.* Fig. 1b).

In summary, both approaches emphasized that propagation effects for more distant source regions within the reach of our study

Downloaded from https://academic.oup.com/gji/article-abstract/211/3/1640/4209579
by Staats- und Universitätsbibliothek Hamburg user
on 19 December 2017

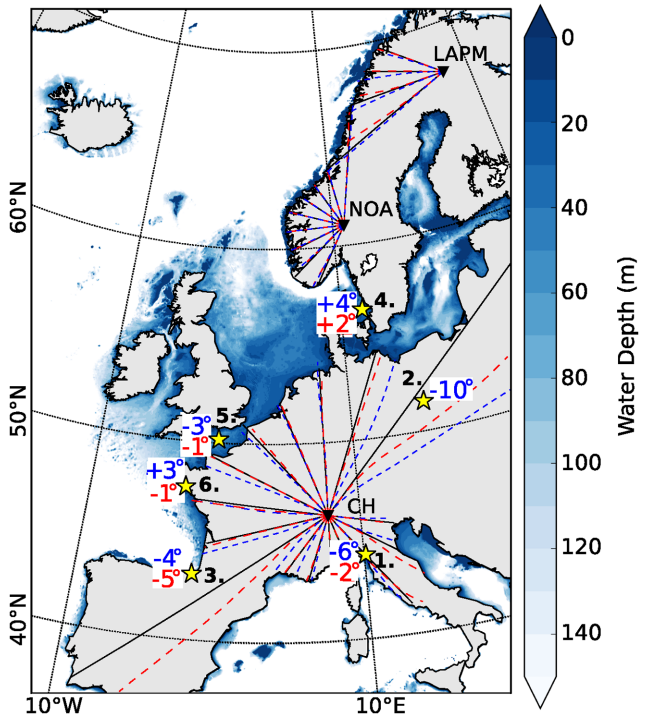

Figure 3. With respect to the CH array centre, differences between event backazimuth as estimated from the great circle path and from beamforming in degrees (positive sign for clockwise deviation) (red: Love wave; blue: Rayleigh wave). Black labels indicate event numbers (see Supporting Information Table S1) and yellow stars mark event locations. The water depth (blue colour range: ETOPO1.0 (Amante & Eakins 2009)), with a maximum depth corresponding to approximately 1/2 of the wavelength for deep water ocean gravity waves at a period of 14 s, indicates regions of intermediate and shallow water. For azimuth increments of 20 degrees from the array centre, great circle paths are indicated by black solid lines, and fundamental mode ray paths, using the velocity model of Section 3 at a period of 14 s are indicated by red (Love wave) and blue (Rayleigh wave) dashed lines.

are not negligible. Additionally, for certain source azimuths, differences in relative azimuthal noise strength between the wave types could arise due to focusing effects, great circle path deviations and changes in polarization, caused by the crustal structure.

Further knowledge of the small scale structure, suitable for short period surface wave simulations, would be needed to overcome this bias. Here, as a consequence we chose to apply azimuthal binning for our following analyses. The bin size reflects the average accuracy of the propagation direction retrieved from beamforming.

4 CORRELATION BETWEEN PRIMARY MICROSEISMIC NOISE AND OCEAN WAVE HEIGHT

In order to constrain the source locations of our noise observations, we compare ocean wave heights with the beamforming results. We obtained open access ocean-wave parameters from resources detailed in Ardhuin *et al.* (2011) which were modelled with WAVEWATCH III® (Tolman 1991; Ardhuin *et al.* 2010). In particular, we use the directionally integrated ocean surface elevation power spectral density $E(f)$, gridded at 3 hr time intervals and at 0.5° Latitude and Longitude increments. The Earth's surface around each array centre was discretized symmetrically into bins of 100 km distance and 8° of azimuthal width overlapping by 25 per cent. For each bin, the spatial mean of $E(f)$ over all included grid points is collected in a time series at period bins around approximately 12.5, 13.8, and 15.1 s averaged over 6 hr. Using smaller temporal increments of 3 hr, did not change our results.

Likewise, we form time series of the maximum direction dependent polarized noise PSD $P(f, \theta)_{\max}$ from beamforming, within each azimuthal bin and for the slowness range indicated in Fig. 1(a) at corresponding period bins. Here, the azimuthal binning is performed to account for travel path deviations, such as estimated in the previous section, but also for array mislocalizations, for example, due to inhomogeneous structure beneath the array.

For each noise-source direction and earth-surface bin combination, the corresponding time series are self-normalized and correlated with each other. Testing the common Pearson correlation coefficient generally indicates a good agreement between the two parameters in coastal regions. However, we use Kendall's Tau (Kendall 1938), for testing the joint monotonous variation of both parameters in this study. The importance of using non-parametric techniques in the context of noise-ocean parameter correlation was recently emphasized by Craig *et al.* (2016). Unlike the Pearson correlation coefficient, Kendall's Tau correlation is robust against outliers and does not assume a linear relation between the two variables. In the presence of multiple sources, as it is usually the case for ocean generated noise, the beampower estimate can be biased unpredictably, which also requires a more robust measure of correlation than comparing actual amplitudes. We estimate the correlation of the two time series $\mathbf{x}$ and $\mathbf{y}$ by Kendall's $\tau_b = (C - D)/\sqrt{(C + D + T_x) * (C + D + T_y)}$, where C and D are the number of concordant (e.g. $x_i > x_k$ and $y_i > y_k$) and discordant ($x_i > x_k$ and $y_i < y_k$) pairs of the time series, respectively. T_x and T_y are the number of ties of either ($x_i = x_k$) or ($y_i = y_k$). Hence, τ_b ranges between -1 and 1, indicating perfect anti-correlation and perfect correlation, respectively.

Results for the different period ranges tested are very similar to each other, hence Fig. 4 shows these correlation maps for a period of 14 s for the arrays NOA, CH and LAPM. We interpret highest correlation coefficients as indication of especially clean source regions, where ocean state and noise state variations at the arrays are closely linked throughout the year. As expected from theory and in agreement with Fig. 1, best correlation coefficients are found in near coastal areas, which correspond to backazimuths of peaks in the azimuthal noise strength distribution. Regions including strong local maxima of the correlation coefficient are marked by boxes in Fig. 4. The geographical distribution of high correlation coefficients for Love and Rayleigh waves are more similar to each other, than the azimuthal beampower back-projections in Fig. 1. Likely, because propagation path effects are of less importance in the binned correlation approach.

The extent of the regions showing high correlation coefficients is mostly larger than areas of shallow water we would like to resolve. Partly because less resolution is achieved along the back-projection direction. But also due the spatial correlation of ocean wave parameters, which increases the width of a point source to a larger area in the correlation maps. Craig *et al.* (2016) suggested to consider autocorrelation maps to obtain an estimate of the spatial correlation of the model parameter. Therefore, we calculate the mean Kendall's Tau correlation coefficient between the yearly ocean wave elevation time series of a data grid point and its surrounding grid points within different distance radii, increasing in 100 km increments. As consequence, we obtain the distance range at each location, for which ocean parameter data is well correlated in space (Kendall's Tau mean above 0.8). This is performed for all centre points on a

Downloaded from https://academic.oup.com/gji/article-abstract/211/3/1640/4209579
by Staats- und Universitätsbibliothek Hamburg user
on 19 December 2017

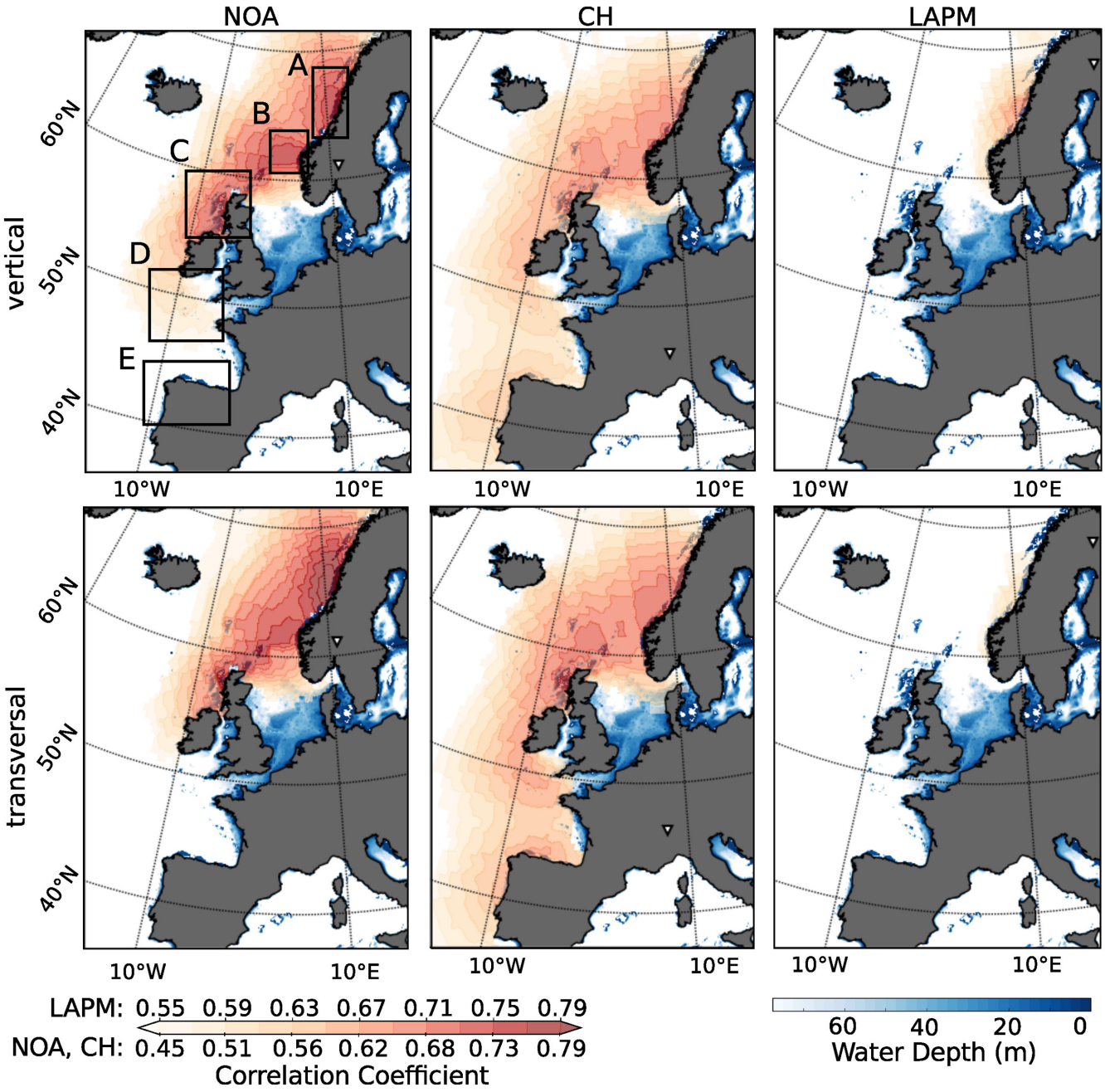

Figure 4. Correlation coefficients (red colour range) between noise and ocean surface elevation at different array sites (triangle: array centre) and a period of 14 s for vertical and transversal component noise observations; and water depth in the background (blue colour range). Boxes (A–E) mark different regions mentioned in this study.

grid with Longitude and Latitude increments of 2°. Figs 5(a) and (b) show a comparison between map views of autocorrelation ranges and of mean yearly ocean surface elevations at a period of approximately 14 s, respectively. The correlation ranges in Fig. 5(a) are relatively large near Norway and Spain, that is, more than 500 km, but smaller near the British Isles and in regions where Islands scatter the ocean waves (compare with Fig. 5b). The spatial correlation of ocean wave parameters seems to be an major limitation for noise source localization as shown in Fig. 4 with this approach. However, the spatial resolution estimate in most coastal areas suggests reliable localizations of source areas which contribute most to the noise levels of the two different wave types.

Highest correlation coefficients in Fig. 4 do, on average, not only correspond to coastal sections with the largest ocean wave heights. The shallow water regime is an important condition for primary microseismic noise generation ($kh \ll 1$), with the water depth h from the ETOPO01.0 data set (Amante & Eakins 2009) and the wave number of ocean gravity waves k (Hasselmann 1963). Therefore, taking the water depth into account provides a better source strength proxy. We scale the mean of $E(f)$ from Fig. 5(b) with $1/\cosh(kh)$, which was referred to as hydrodynamic filtering factor by Fukao *et al.* (2010). The local ocean gravity wave number k was calculated via the Airy wave theory dispersion relation $\omega^2 = g\,k \tanh(kh)$, with the angular frequency of ocean gravity waves ω and the gravitational

Downloaded from https://academic.oup.com/gji/article-abstract/211/3/1640/4209579
by Staats- und Universitätsbibliothek Hamburg user
on 19 December 2017

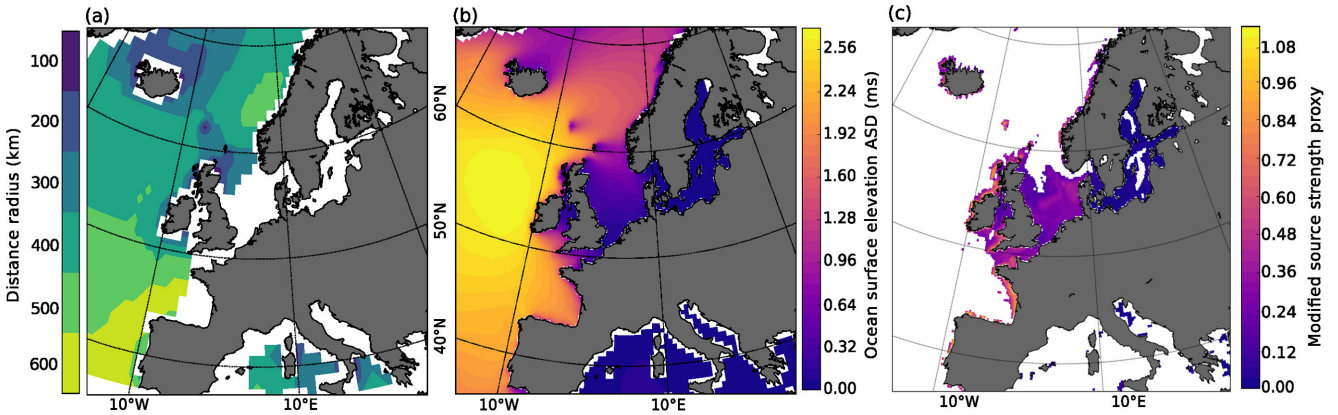

Figure 5. (a) Map view of the distance range at each location within which the model data have an average CC above 0.8. (b) Average ocean surface displacement PSD at a period of approximately 14 s in 2013. (c) Average seismic source proxy of wave height scaled by water depths.

acceleration $g = 9.81\ \mathrm{ms}^{-2}$. Most important source areas in 2013, as marked in Fig. 4, are in accordance with this modified source proxy in Fig. 5(c). We will study one of them, the Norwegian source regions, in more detail in the next section and focus on differences between Love and Rayleigh waves observed from these locations.

5 ARRAY BASED LOCALIZATION

We exploit the vicinity of the Norsar and the Lapnet array to the Norwegian coastal source regions in order to constrain their location more accurately. Due to low ratios between source distance and array aperture, the plane wave assumption is often violated for these source regions. Therefore, we are able to use a curved wave-front approach to estimate the source distance in addition to direction by beampower maximization. We test whether the velocity model of Section 3 is accurate enough to estimate traveltime differences for surface waves in the period range of interest, using the larger Lapnet array, which spans over a few grid points of the velocity model. Fig. 6(a) shows wave fronts corresponding to the fundamental modes of both wave types at a period of 14 s using the velocity model with respect to a test source location (star). Comparing resulting beampowers of this approach, to one which uses a homogeneous velocity model, shows no improvement. Therefore, beamforming phase shifts are applied according to assumed regular wave-front curves corresponding to a homogeneous velocity model, with origin distance increments of 50 km. We do not attempt to locate surface wave signals from more distant locations than the Norwegian coast and disregard such time windows for this analysis. Since the resolution capability of the localization decreases with source area size and superpositions of sources, we disregard extended sources by excluding beamformer maxima which are smeared out in azimuth and distance. We consider source positions which were localized at least twice during the given winter month periods.

Detailed localization results for a sequence of individual time windows during few days in February 2009 can be found in the Supporting Information. Here, we show a localization stack for the total time span analysed. Figs 6(a) and (b) shows source localizations of the strongest Rayleigh wave (vertical component) and Love wave (transversal component) noise signals, respectively, along the Norwegian coast. The colour of the markers represents results of the corresponding array and its time spans (Norsar: November–December 2013; Lapnet: December 2008 to February 2009).

An interesting observation is that, independent of the highest swell distribution, specific locations are responsible for the most frequent strongest noise generation. During both time spans, we locate a dominant source region near 65°N and 11°E (in region A) for both wave types. Although primary microseismic noise is also generated directly to the west of the Norsar array (region B), region A produces higher noise amplitudes for Love wave signals observed at this array. Both arrays indicate a slight difference in source position near 65°N and 11°E. Considering the velocity model at hand, this difference could be explained by propagation path effects for the Lapnet array (*cf.* Figs 3 and 6a). For the Norsar array the observed deviation is minor and also propagation path effects were estimated to be small.

Using a German array, Matsuzawa *et al.* (2012) tracked microseismic noise generated by a storm, propagating along the Norwegian coast, at a period of 20 s. They found that Love waves originated from a more confined and more eastern azimuthal range compared to Rayleigh waves. Via ray tracing, the authors refuted propagation path effects as explanation for the wave-type difference. They instead interpreted them as indication of different source locations. In our analysis, with arrays near the Norwegian coast, we do not find independent source locations, but observe spatial differences in source localization rate for each wave type with more spatial variability for Rayleigh waves. The observations in this section suggest a difference in the efficiency with which each wave type is generated in different regions or observed from these regions.

6 LOCAL NOISE GENERATION EFFICIENCY FOR DIFFERENT LOCATIONS

We analyse the spatial dependence of the relation between local ocean wave heights and microseismic noise amplitudes of both wave types. Therefore, we compare the time series of azimuth dependent noise amplitude spectral density $\sqrt{P(f,\theta)_{\max}}$ from beamforming and vertical ocean surface displacement spectral density $\sqrt{E(f)}$ from the ocean model. Both time series are averaged over 6 hr. Since the data is analysed in a narrow period band at approximately 14 s, we take $\sqrt{P(f,\theta)_{\max}}/i\omega$ for comparison between vertical displacements. The microseismic noise amplitudes are obtained from azimuthal bins θ_m with high relative beampowers at the Norsar array. Ocean wave heights are taken from the nearest ocean data bin in the corresponding directions. Figs 7(a) and (b) shows the relation

Downloaded from https://academic.oup.com/gji/article-abstract/211/3/1640/4209579
by Staats- und Universitätsbibliothek Hamburg user
on 19 December 2017

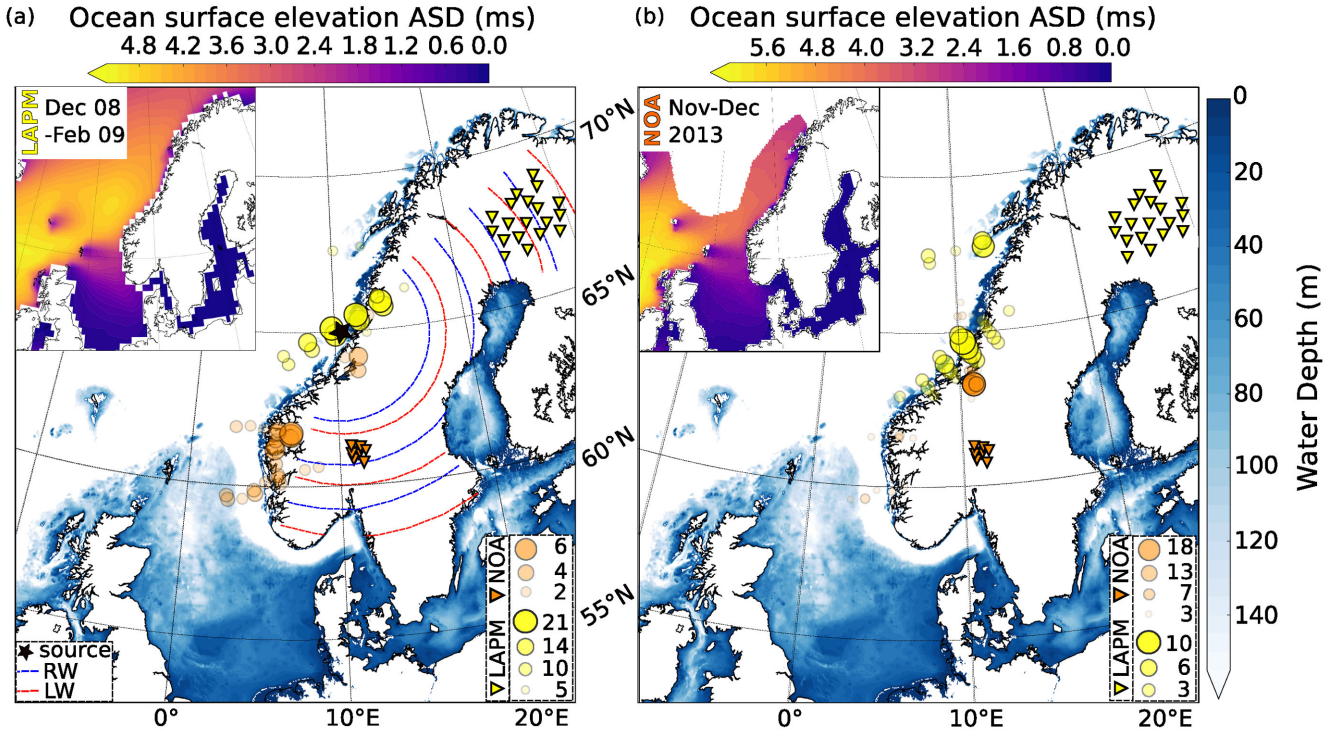

Figure 6. Map view of number counts of source positions (circle size) for vertical component (a) and transversal component (b) noise observations from the curved wave-front beamforming localization with the Norsar array (orange) and the LAPM sub-array (yellow). Insets: Ocean surface elevation spectral density at a period of approximately 14 s averaged over the indicated time spans, corresponding to the LAPM data period in inset (a) and the Norsar data period in inset (b). In (a), dashed lines indicate wave fronts of the fundamental modes of both wave types from ray tracing with the velocity model of Section 3, originating from the location marked by the star.

between both time series for two ocean bin locations as indicated in the map in Fig. 7(c).

Depending on the sea-floor topography some directional parts of the ocean wave spectra could contribute more to seismic noise generation than others. Since we used the directionally integrated parameter E_f we neglected this directional information here, which likely contributes to the spread in the parameter relation. However, in the observed range, the relation between ocean surface elevation and seismic-noise amplitude spectral density is of approximately linear character for both wave types. This agrees with the theoretical understanding of Rayleigh wave generation, as detailed by Hasselmann (1963) and by Ardhuin *et al.* (2015), and with several previous observations at sufficient distance from the source area (e.g. Barruol *et al.* 2006; Young *et al.* 2012).

By a least-squares approach we fit linear functions ($\sqrt{P(f)} = L + T\sqrt{E(f)}$) to the parameter relations, corresponding to all regions with Kendall's Tau coefficient above 0.55. As additional measure of source quality and of linear curve approximation validity, we use the mean relative residuals, and set an upper reliability threshold of it to 0.25. We relate the slope T (or transfer factor) with the efficiency of generated microseismic noise strength, observable at an array, due to a given ocean wave height within a source location bin. L is interpreted as random background noise level at the array. Map views of the resulting transfer factors T for both wave types, and corresponding mean normalized residuals are shown in Fig. 8.

As expected, areas with low residuals (dark colours), which are approximated best by the linear curve, coincide with highest correlation coefficients (Fig. 4) and with relative noise strength peaks (Fig. 1). For some backazimuths with respect to an array, several different coastal regions are located along the same great circle path direction. If the distance difference is small, the further source is not eliminated by attenuation, and source mixing likely decreases the correlation coefficient and linear character of the relation. This is especially obvious in the case of CH results for distant coasts. Nevertheless, for directions with a single possible source region nearby, we expect it to dominate the noise observation from that specific direction. For these regions, we can identify a close link between the ocean state and noise state variations.

The highest values for efficiency T are obtained for specific coastal sections and do generally correspond to low mean normalized residuals. Parts of the surface bins used include more shallow water area, where ocean surface elevations are on average lower than in deeper water. The efficiency could be biased in these cases. Nonetheless, despite the possible overestimation, low relative residuals distinguish these regions as especially bright sources. Further, attenuation is expected to decrease T with distance to the source. Remembering these limitations, we concentrate on the relative comparison between the wave types. For both, we note that the transfer factor T and the linearity depend strongly on location. The most clean and efficient noise generating regions are found at coasts near Norway and the northern part of the British Isles (regions A, B, C). However, for Love wave measured at NOA from regions B and C we find lower efficiencies than for Rayleigh waves. On the other hand, the Norwegian coast area (region A), which was found to be a frequent source area with the array based localizations, shows a cleaner source signature and efficiency for Love waves than for Rayleigh waves. Similar to higher relative noise amplitudes, the relative source brightness for Love waves observed with CH is higher at coasts near Spain and France. These differences between the wave types could be imposed by earth structure but also by generation

Downloaded from https://academic.oup.com/gji/article-abstract/211/3/1640/4209579
by Staats- und Universitätsbibliothek Hamburg user
on 19 December 2017

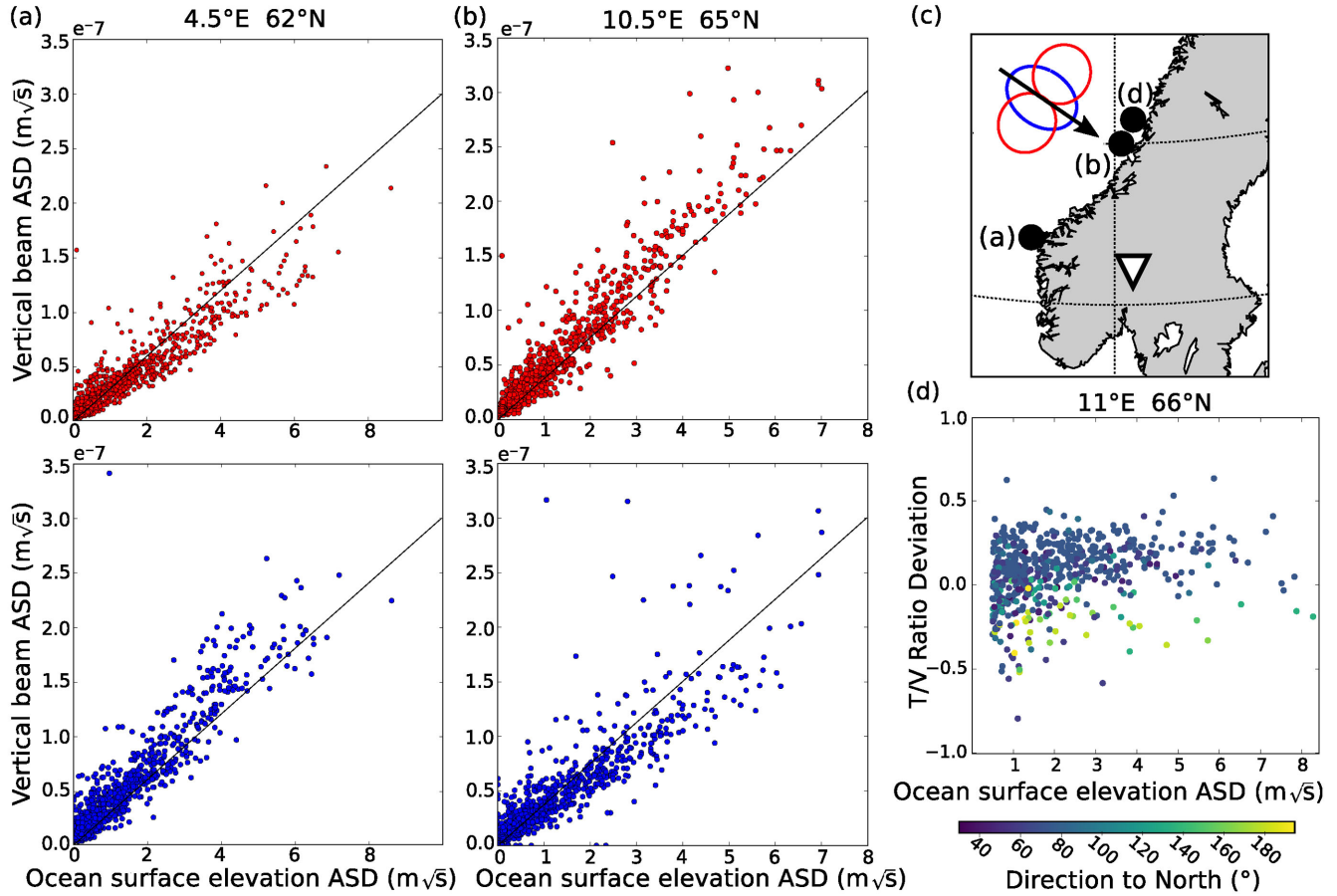

Figure 7. (a,b) Relation between seismic noise and ocean surface elevation ASD for two locations of high correlation coefficient using Norsar array measurements. (c) Map indicating ocean parameter data locations for subplots (a), (b) and (d) of this figure. Schematic illustration of the radiation pattern of Love waves (red) and Rayleigh waves (blue) due to a superposition of a vertical and a horizontal single force (black arrow). (d) Relation between transversal/vertical noise ratio versus ocean surface elevation ASD. Colour range: Ocean gravity wave propagation direction with respect to north (clockwise).

conditions in the source area. In the following section we will study the influence of properties in the source region, especially the so far neglected effect of swell direction.

7 DEPENDENCE ON SOURCE REGION PARAMETERS

The ability to explain observed amounts of seismic motion for transversal and vertical/radial polarizations is a requirement for understanding the process of primary microseismic generation entirely. Previously, different authors discussed primary microseism source processes in addition to pressure type sources (Hasselmann 1963), that feature horizontal tractions, capable of generating both wave types simultaneously.

On one hand, such a generation of both wave types was suggested for certain conditions, with different radiation patterns for Love and Rayleigh waves (Friedrich *et al.* 1998; Saito 2010). For example, ocean gravity waves propagating across the shallow surf zone at shores or across regular topography patterns, likely cause directed shear tractions. These could excite most energetic Rayleigh wave radiation either symmetrically or dominantly parallel with respect to the ocean wave propagation direction or with respect to sea-floor gradients, while Love waves can be expected to radiate strongest towards perpendicular directions (e.g. Friedrich *et al.* 1998; Saito 2010; Ardhuin *et al.* 2015). A corresponding wave type radiation pattern for this scenario is illustrated in Fig. 7(c).

On the other hand, the relative strength of multiple source mechanisms (pressure versus shear sources) could vary differently in dependence on the swell direction. For both of these cases, a variation of the wave-type ratio, observed at a fixed location, could be expected for varying ocean-wave propagation directions. Hence, the polarization type noise ratio can hold information about generation processes. We test the dependence of observed Love to Rayleigh wave noise ratios on ocean wave parameters.

7.1 Ocean wave propagation direction

For selected locations around Europe, at the 300 m depth contour, modelled full ocean wave directional spectra are available from open data resources described in Ardhuin *et al.* (2011) and Ardhuin *et al.* (2015). Additionally, model output at several buoy locations was available. Both data sets were obtained for locations of interest. A time series of ocean wave propagation direction relative to North corresponding to the spectral peak at a desired frequency, discretized in steps of 15°, is extracted with 6 hourly increments similar to the parameters in Section 4. The time series of this peak direction is linked with the wave-type ratio. Fig. 7(d) shows the demeaned transversal/vertical component noise amplitude spectral density ratio using Norsar array observations versus ocean surface elevation

Downloaded from https://academic.oup.com/gji/article-abstract/211/3/1640/4209579
by Staats- und Universitätsbibliothek Hamburg user
on 19 December 2017

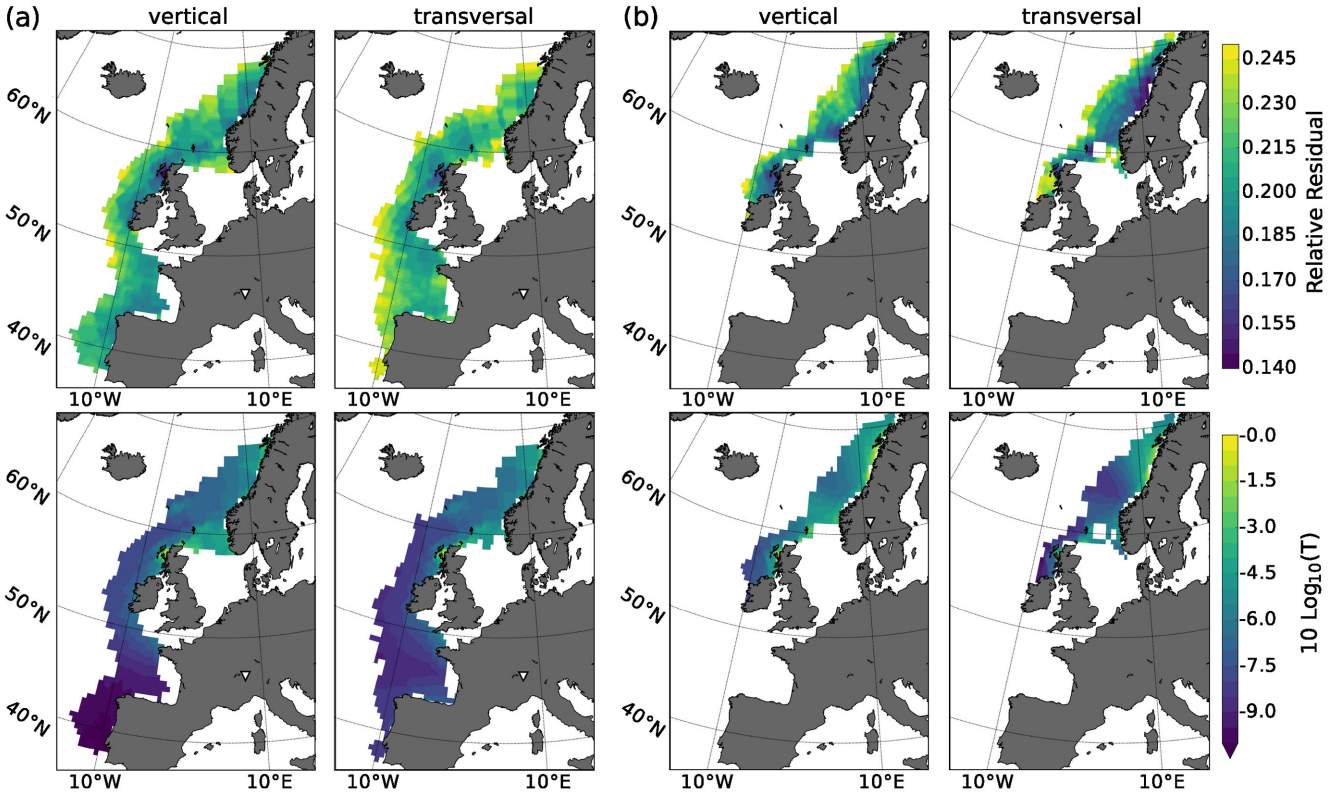

Figure 8. Map view of mean relative residuals (top; colour range) and corresponding relative values of T from linear function fits (bottom; colour range) for vertical and transversal beamformer results observed at the Swiss array (a) and at the Norsar array (b).

spectral density at an example position as marked in Fig. 7(c). The colour range of the data points indicates peak propagation direction. Here, measurements corresponding to wave heights lower than 0.5 m were excluded, since microseimic noise levels did not significantly rise above the background level at the array. We observe a separation of wave-type ratio with the peak direction (darker and lighter colour). The wave-type ratio for similar peak directions remains relatively stable over the observed ocean wave height range. The characteristics shown here, are representative for the majority of test locations along the coasts.

For a detailed analysis of the wave-type ratio modulation in Fig. 7(d), we directly plot ratio versus ocean wave direction Figs 9(a) and (b) show the demeaned transversal/vertical component PSD ratio at the arrays NOA and CH versus peak ocean wave propagation direction at the near-coastal locations which show high correlation coefficients and linear relation approximation. For each given location, the ratio varies with ocean wave propagation direction in a harmonic manner. In order to find the peak propagation directions corresponding to the extrema of the data, we fit a sine (red dashed line) to the mean ratio data points (red dots). Figs 9(c) and (d) show map views of the ocean wave directions corresponding to the minimum (blue) and maximum (red) transversal/vertical component noise ratio, as determined by the fitted function. We observe a difference of approximately 90° between the extrema. Transversal/vertical component ratio minima occur mainly for peak ocean wave propagation directions towards the observation point and maxima occur for ocean wave directions perpendicular to it. This would agree with an imprint of a source mechanism that depends on swell direction.

The insets for each array in Figs 9(c) and (d) show histograms of the fit function period from all locations. For noise measurements at both arrays, the period shows a peak around 190°. We note that using peak ocean wave direction is a simplification, since the shape of the full ocean wave directional spectrum is not accounted for. Additionally, ocean wave directions in the shallow water area ($h \leq$ 40 m) and in 300 m of water depth likely differ to some extent. Despite this, results for different locations show consistency and the periodicity distribution peaks agree with the average angular difference between the ratio extrema of 90°.

From the point of view of a single array it is difficult to determine whether the wave type ratio modulation depends on swell propagation direction with respect to the coastline. Since different authors discussed the possibility of primary microseismic source mechanisms that feature specific radiation characteristics for Love and Rayleigh wave energy (e.g. Friedrich *et al.* 1998; Saito 2010), we test our wave type ratio data against an imprint of these source radiation models. In order to evaluate the possibility of such a dependence we test the symmetry orientation of the wave type ratio variation. We use Norsar array measurements of the wave-type ratio in different azimuthal bins and compare them to peak ocean wave propagation directions at locations marked by circles in Fig. 10(c). We form ratio medians for corresponding ocean propagation directions within relative angular increments of 15° for two different symmetry orientations (a) relative to the great circle path direction to the array and (b) relative to the coast normal. Results are shown in Figs 10(a) and (b), respectively.

We evaluate the degree of correlation between both parameters, with the non-parametric Kendall's Tau coefficient, and transfer the result to grey scales indicating perfect correlation (1: black) and no correlation (0: white). Fig. 10(c) shows these values as colour range filling the marker symbols. We find a higher degree of correlation for symmetry orientation (a). Lower Love

Downloaded from https://academic.oup.com/gji/article-abstract/211/3/1640/4209579
by Staats- und Universitätsbibliothek Hamburg user
on 19 December 2017

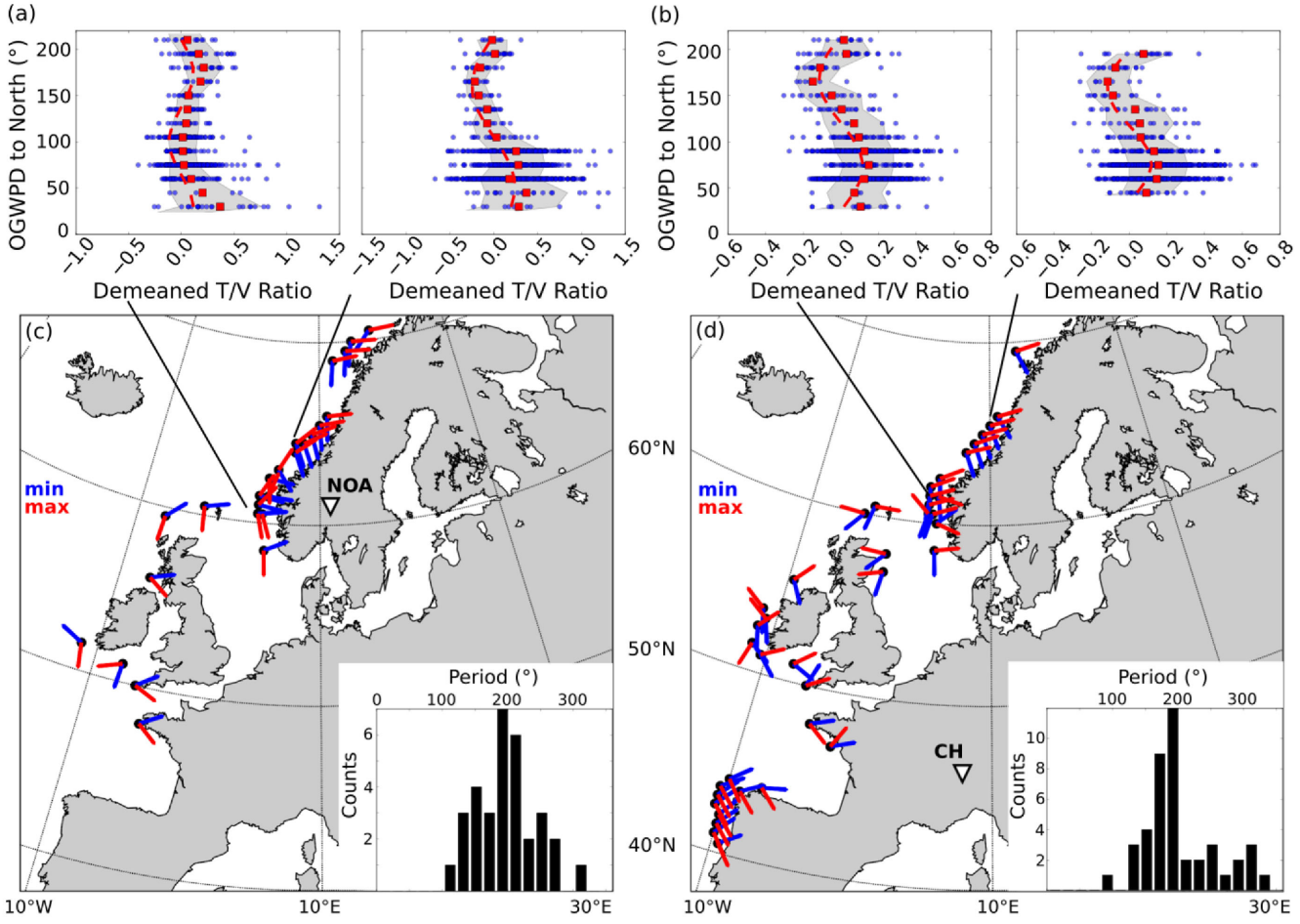

Figure 9. (a,b) Blue dots: Demeaned transversal/vertical component noise ratio at two arrays (NOA for (a), CH for (b)) versus ocean gravity wave propagation direction (OGWPD) at indicated locations (lines) at a period of 14 s; red dots: data means; gray area: 1σ range; red dashed line: fitted sine. (c,d) Map views of OGWPD corresponding to minimum (blue) and maximum (red) transversal/vertical noise ratios. Insets: Histograms of fit function periods at a periods 14 s.

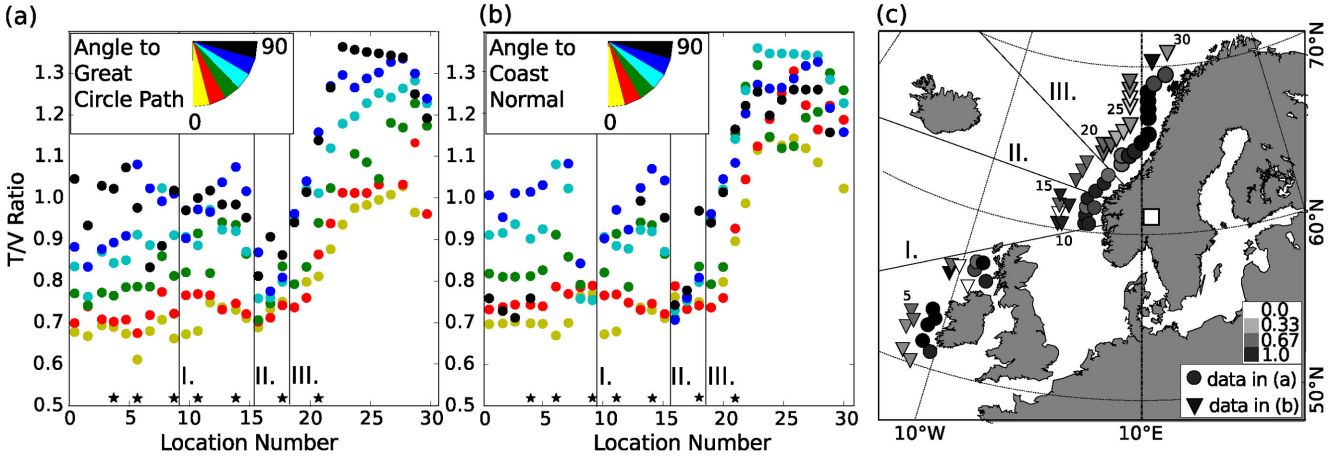

Figure 10. Relation between transversal/vertical noise ratio versus ocean gravity wave propagation direction at different locations from the Wavewatch model output located at the 300 m depth contour and at buoy locations (black stars) with respect to the great circle path direction (a) and to the local coast normal (b). (c) Corresponding locations (circles) with correlation coefficient between noise ratio and ocean propagation direction increments in gray scale, indicating Kendall's Tau values from 1 (black) to 0 (white) for case (a) and (b). Triangle symbols for case (b) were shifted from their original location for visibility.

to Rayleigh wave ratios could be expected when most energetic ocean waves propagate directly onto coastal slopes. In that case, the shoaling mechanism for Rayleigh wave excitation proposed by Hasselmann (1963) likely increases relative to possible other generation mechanisms. However, our observations indicate a more direct dependence of the wave-type ratio modulation on peak ocean wave propagation directions than their propagation relative to the coast.

Downloaded from https://academic.oup.com/gji/article-abstract/211/3/1640/4209579
by Staats- und Universitätsbibliothek Hamburg user
on 19 December 2017

We find that the average wave-type ratio level differs for coastal sections in Fig. 10 (marked sections I, II, and III). This hints to additional constraints for the generated proportions of the different wave types. One likely cause for this observation are bathymetric conditions that differ for the corresponding locations causing difference in importance of potential multiple mechanisms. Another possibility would be the character of the coast. For instance in the case of a straight coastline (e.g. region A and E), where sources are aligned along a large portion of the coast, the ratio pattern of the wave type radiation would translate into the observations, but average out for a random source orientation at a chaotic coast line (e.g. region C).

7.2 Bathymetry

For a period of 14 s the deep water ocean gravity wave length λ is approximately 300 m according to the Airy wave theory dispersion relation. In the period range considered here, the shallow water regime corresponds to depths h of a few tens of metres and less. Hence, efficient primary microseism generation should occur within a narrow region of coastal shallow water, Fig. 5(c).

By analysing which regions correspond to the highest relative beamformer amplitudes Fig. 1, correlation coefficients (dark colours in Fig. 4), and efficiency factors (light colours in Fig. 8), we find the following characteristics: (1) the most important noise contributions from the Norwegian coast (region A, B) as well as from the Scottish coast (region C) originate from regions with extended shallow water areas including several small islands and fjords. (2) clearly lower correlation coefficients are obtained for the Celtic sea south of Ireland (region D), a region of average deeper water, which includes sea-mount topography raising below few tens of metres in water depths. (3) From the Spanish coast (region E), comparably high Love waves levels are observed, compared to Rayleigh waves. This coastal region includes both, shallow water as well as steep sections. An array near this area would be desirable for a confinement of source regions there. On the other hand, relatively high Love to Rayleigh wave signal ratios observed from regions A and E, and might be an indication for favourable bathymetry conditions for shear tractions in these regions. In summary, these observations agree with studies, which suggest a strong influence of topography on noise generation effectivity (e.g. Fukao *et al.* 2010; Saito 2010; Ardhuin *et al.* 2015).

7.3 Testing the source imprint

Wave propagation in complex earth structure influences the relative content of different surface waves in the microseismic noise field. However, high Love to Rayleigh wave energy ratios, and similar azimuthal modulation of wave-type ratio at different European array sites (Juretzek & Hadziioannou 2016) suggests an additional imprint of source processes onto observations. Since primary microseimic noise is possibly generated by multiple mechanisms (Friedrich *et al.* 1998), the relative strength of individual mechanisms could differ with region, for example, due to bathymetric conditions. Still, our observations in Section 7.1 cannot easily be explained by such static causes alone. They likely hint towards a dynamic effect, for example, a mechanism ratio that is ocean swell direction dependent or towards an imprint of directive wave-type radiation.

In order to estimate if such effects qualitatively fit our observations, we use Instaseis (van Driel *et al.* 2015) with the radially symmetric 1-D anisotropic PREM model. We calculate vertical and transversal component seismic displacement RMS amplitudes at the centres of the Norsar and Swiss array in response to different force field distributions. To be able to separate the differently polarized wave types simply by radial and transversal components, we separately calculate the seismic response to sources within azimuthal windows of 8° width.

Since detailed information on shallow water bathymetry would be required for a quantitative evaluation of the source terms, we apply general proportionality assumptions for magnitudes of shear traction and pressure type sources. Following Gualtieri *et al.* (2013) we use single forces representing extended shear traction or pressure source fields within spatial grid cells near coastal regions ($h \leq$ 100 m). We apply a distribution of horizontal and vertical forces which are proportional to local wave heights. Additionally we take force strengths to scale inversely proportional with water depth, specifically with $1/\cosh(kh)$ (e.g. Fukao *et al.* 2010).

Since the PREM model does not provide realistic attenuation properties at our frequencies of interest, we use the correlation coefficients between microseismic noise and ocean wave heights, determined in Section 4, to empirically approximate the maximum distance of source sensitivity for an array. Therefore, we disregard source locations outside regions with a correlation coefficient $\geq$0.4.

We use the yearly mean of modelled wave heights in 2013 at a period of 14 s as mean source strength distribution proxy and interpolate the data onto the same grid which is used for scaling with water depth. We estimate the azimuthal pattern of wave-type ratio generated by the spatial distribution of co-located vertical and horizontal forces with H/V force ratio of 1.1. We choose three different settings for horizontal force orientations: (1) normal to the smoothed European continental coastline, (2) aligned with most frequent peak ocean wave propagation direction near coasts during 2013, and (3) purely random orientations. In case (1) and (2) we use a half sided cosine with 180° periodicity for an angular force modulation of 80 per cent around the main force orientation (see inset in Fig. 11). In case (3) we increase the H/V force ratio within region A and E to 1.4.

Fig. 11 shows the transversal/vertical amplitude ratios at both array centres for the 3 test settings. By comparing our estimated azimuthal wave-type ratios to observations in Fig. 1, we find that the swell direction dependent force orientation as well as a regional increase in H/V force ratio reproduce azimuthal wave-type dominance qualitatively. An imprint of directed horizontal forces normal to coasts does not fit our observations. Additionally, for an inclusion of detailed coastline roughness for this case, we envision an effective randomization of the force orientation and less agreement with direction dependent ratio observations.

8 DISCUSSION

In this study we observed that primary microseimic noise of both Love and Rayleigh waves, correlates well with modelled ocean wave heights in near coastal areas. This meets with expectations from the theoretical understanding of primary microseismic noise generation and is in accordance with previous observations (e.g. Bromirski *et al.* 1999; Barruol *et al.* 2006; Ardhuin *et al.* 2015). Regions of highest correlation coefficient coincide between the wave types (*cf.* Fig. 4), which agrees with our observations that Rayleigh and Love waves mainly propagate from similar directions as shown in Fig. 1.

Our measurements showed a linear relation between noise and vertical ocean surface displacement spectral density in near coastal

Downloaded from https://academic.oup.com/gji/article-abstract/211/3/1640/4209579
by Staats- und Universitätsbibliothek Hamburg user
on 19 December 2017

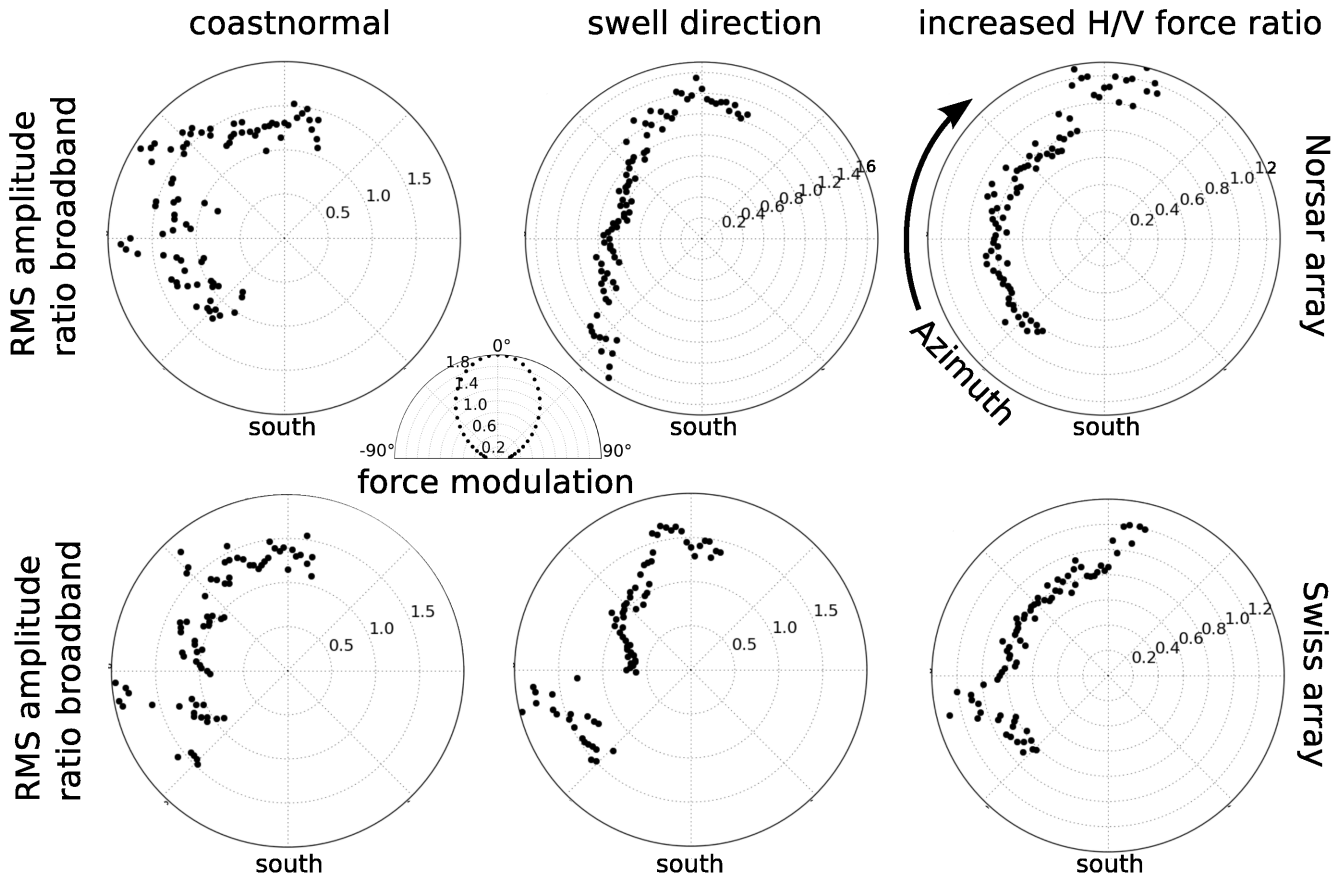

Figure 11. Modelled transversal/vertical component RMS displacement amplitude ratios (radial axis) versus source azimuth observed from the array centres for three different test cases. The direction dependent horizontal force modulation around a test orientation is shown in the inset.

areas. This enabled the localization of regions which act as especially bright source areas for the different arrays. Most efficient source regions found here (e.g. the Norwegian coast and the British Isles), agree with locations which were identified as strong primary microseismic sources for Rayleigh waves in previous studies (e.g. Friedrich *et al.* 1998; Möllhoff & Bean 2016; Sadeghisorkhani *et al.* 2016). However, we also found that noise generation efficiency is location dependent (Fig. 8), in agreement with observations by Barruol *et al.* (2006), and appears to differ for Love and Rayleigh wave type noise from several areas. This agrees with azimuthal variations in the wave-type ratio, which were observed previously (Juretzek & Hadziioannou 2016). Both coinciding source azimuths between the wave types and a stable wave-type ratio with ocean wave height variations (Fig. 7d) argue against entirely independent generation mechanisms and source regions of Love and Rayleigh wave primary microseismic noise.

Structural effects (e.g. focusing, waveguide interruption, change in polarization, etc.) likely influence observations of primary microseismic noise signals. Estimates of propagation path deviations within paths to nearby source regions in this study, propose that theoretical and observed backazimuths can deviate up to the order of tens of degrees from each other, in agreement with previous studies. Hence, structure should be considered in more detail in future studies in complex or far inland terrain. An estimate of potential secondary generation of Love waves through conversions from Rayleigh waves, especially occurring near or in the source region, is not within the scope of this study. This option and the influence of sedimentary layers and crustal heterogeneities at the ocean-continent transition on surface wave amplitudes (e.g. McGarr 1969) is not considered in many studies and remains to be evaluated. However, observations from arrays at different geographic locations suggest that local source region properties seem important for noise generation efficiency differences and for wave-type ratio differences.

One likely important factor for both the source efficiency differences and for the wave-type ratio, is the local bathymetry present in the source areas. The effect of the shallow surf zone on noise generation strength was also estimated to be significant by Hasselmann (1963) earlier. This bathymetry influence was also supported by the work of Fukao *et al.* (2010), who showed how ocean gravity waves in deep water could generate Love and Rayleigh waves simultaneously in the hum frequency band when seafloor topography is present. We cannot confine source regions accurately enough to clearly evaluate particular bathymetry types. However, the regions for which we obtain peaks for the correlation coefficient as well as for the efficiency, often correspond to areas of extended shallow water depths with topography and islands.

Love wave generation may be possible through horizontal tractions due to ocean wave movement (Friedrich *et al.* 1998; Saito 2010; Ardhuin *et al.* 2015). Here, we found a correlation between the transversal/vertical component noise ratio and peak ocean wave propagation direction. This rather hints towards generation of both wave types in the source region and towards time dependent conditions for the excitations efficiency of each wave

Downloaded from https://academic.oup.com/gji/article-abstract/211/3/1640/4209579
by Staats- und Universitätsbibliothek Hamburg user
on 19 December 2017

type. Our observations of a link between wave-type ratio and peak ocean wave propagation direction (Fig. 9) is an indicator for this possibility. One likely important cause for efficiency differences and ratio differences is an effective wave-type radiation pattern from the source area, for at least one of the wave types. Another possibility would be a varying importance of different source mechanisms in dependence on swell direction.

An anisotropic wave type radiation and a time dependent wave type excitation strength could be enabled by bathymetric filtering conditions and by a link between shear traction strength and ocean wave propagation conditions (Saito 2010; Ardhuin *et al.* 2015). Considering high resolution topography characteristics on the scale of ocean gravity wave lengths will be required in order to answer these questions.

9 CONCLUSIONS

By means of beamforming and correlation of noise amplitudes with ocean surface elevation we studied how primary microseismic noise source areas of Love and Rayleigh waves compare with each other. We found that beamformer results as well as correlation with ocean surface elevation showed differences between noise strengths of the wave types emitted from the same coastal sections. Further, some parts of the coast serve as especially bright sources of Love waves, meaning that the relation between ocean parameters and noise strength is especially close and that they seem relatively more effective at horizontally polarized noise generation. For Northern and Central Europe, most energetic microseimic noise of both wave types is measured from sources along the coasts of Scotland and Norway.

We find that both Rayleigh and Love wave noise amplitudes depend similarly on the ocean wave heights, which hints at a joint or coupled source mechanism for the wave types. We observe a correlation between the wave-type ratio and the peak ocean wave propagation direction. This hints towards a dependence of wave type excitation efficiency on swell direction or an effective source radiation pattern. One possible reason for this could be horizontal tractions which are directive in orientation relative to ocean wave propagation.

Observed azimuthal variations in wave type ratio suggest regional differences in the importance of different possible generation mechanisms. This could arise due to different excitation of the wave types dependent on bathymetric conditions but could also be explained by directive wave type radiation. These options is supported by a good qualitative agreement between our synthetic tests and observations. Synthetic tests do not support a dominant imprint of shear forces which are oriented perpendicular to coastlines. Overall, we conclude that the Love to Rayleigh wave ratios carry Supplementary Information about the primary microseism excitation mechanism.

ACKNOWLEDGEMENTS

We wish to thank F. Ardhuin, M. Gal, L. Krischer, S. Mader, H. Sadeghisorkhani, T. Tanimoto, J.-N. Tödt, and D. Ziane for helpful discussions and suggestions for the improvement of this material. We thank M. Afanasiev and A. Fichtner for providing their velocity model. We thank the editor and two anonymous reviewers for comments which helped improve the manuscript. We acknowledge support from and discussions within TIDES COST Action ES1401. This work was funded by the Emmy Noether program (HA7019/1-1) of the German Research Foundation (DFG), and supported through the Cluster of Excellence 'CliSAP' (EXC177), Universität Hamburg, funded by the German Science Foundation (DFG).

REFERENCES

Afanasiev, M., Peter, D., Sager, K., Simutė, S., Ermert, L., Krischer, L. & Fichtner, A., 2016. Foundations for a multiscale collaborative global Earth model, *Geophys. J. Int.,* **204**(1), 39–58.

Amante, C. & Eakins, B.W., 2009. *ETOPO1 1 Arc-minute Global Relief Model: Procedures, Data Sources and Analysis,* US Department of Commerce, National Oceanic and Atmospheric Administration, National Environmental Satellite, Data, and Information Service, National Geophysical Data Center, Marine Geology and Geophysics Division Colorado.

Ardhuin, F. *et al.*, 2010. Semiempirical dissipation source functions for ocean waves. Part I: Definition, calibration, and validation, *J. Phys. Oceanogr.,* **40**(9), 1917–1941.

Ardhuin, F., Stutzmann, E., Schimmel, M. & Mangeney, A., 2011. Ocean wave sources of seismic noise, *J. geophys. Res.,* **116**, C09004, doi:10.1029/2011JC006952.

Ardhuin, F., Gualtieri, L. & Stutzmann, E., 2015. How ocean waves rock the Earth: two mechanisms explain microseisms with periods 3 to 300 s, *Geophys. Res. Lett.,* **42**(3), 765–772.

Aster, R.C., McNamara, D.E. & Bromirski, P.D., 2008. Multidecadal climate-induced variability in microseisms, *Seismol. Res. Lett.,* **79**(2), 194–202.

Barruol, G., Reymond, D., Fontaine, F.R., Hyvernaud, O., Maurer, V. & Maamaatuaiahutapu, K., 2006. Characterizing swells in the southern Pacific from seismic and infrasonic noise analyses, *Geophys. J. Int.,* **164**(3), 516–542.

Beucler, Ã., Mocquet, A., Schimmel, M., Chevrot, S., Quillard, O., Vergne, J. & Sylvander, M., 2015. Observation of deep water microseisms in the north Atlantic ocean using tide modulations, *Geophys. Res. Lett.,* **42**(2), 316–322.

Behr, Y., Townend, J., Bowen, M., Carter, L., Gorman, R., Brooks, L. & Bannister, S., 2013. Source directionality of ambient seismic noise inferred from three-component beamforming, *J. geophys. Res.,* **118**(1), 240–248.

Bromirski, P.D., 2001. Vibrations from the "perfect storm", *Geochem. Geophys. Geosyst.,* **2**(7), doi:10.1029/2000GC000119.

Bromirski, P.D., Flick, R.E. & Graham, N., 1999. Ocean wave height determined from inland seismometer data: Implications for investigating wave climate changes in the NE Pacific, *J. geophys. Res.,* **104**(C9), 20 753–20 766.

Cotte, N., Pedersen, H.A., Campillo, M., Farra, V. & Cansi, Y., 2000. Off-great-circle propagation of intermediate-period surface waves observed on a dense array in the French Alps, *Geophys. J. Int.,* **142,** 825–840.

Craig, D., Bean, C.J., Lokmer, I. & Möllhoff, M., 2016. Correlation of wavefield-separated ocean-generated microseisms with North Atlantic source regions, *Bull. seism. Soc. Am.,* **106**(3), 1002–1010.

Ebeling, C.W., 2012. Inferring ocean storm characteristics from ambient seismic noise: a historical perspective, *Adv. Geophys.,* **53,** 1–33.

Esmersoy, C., Cormier, V. & Toksoz, M., 1985. Three-component array processing, in *The VELA Program. A Twenty-Five Year Review of Basic Research*, Vol. 78, No. 5, pp. 1725–1743, ed. Kerr, A.U., Executive Graphic Services.

Essen, H.-H., Krüger, F., Dahm, T. & Grevemeyer, I., 2003. On the generation of secondary microseisms observed in northern and central Europe, *J. geophys. Res.,* **108**(B10), 2506, doi:10.1029/2002JB002338.

Ferretti, G., Zunino, A., Scafidi, D., Barani, S. & Spallarossa, D., 2013. On microseisms recorded near the Ligurian coast (Italy) and their relationship with sea wave height, *Geophys. J. Int.,* **194**(1), 524–533.

Friedrich, A., Krüger, F. & Klinge, K., 1998. Ocean-generated microseismic noise located with the Gräfenberg array, *Journal of Seismology,* **2**(1), 47–64.

Fukao, Y., Nishida, K. & Kobayashi, N., 2010. Seafloor topography, ocean infragravity waves, and background Love and Rayleigh waves, *J. geophys. Res.,* **115**, B04302, doi:10.1029/2009JB006678.

Downloaded from https://academic.oup.com/gji/article-abstract/211/3/1640/4209579
by Staats- und Universitätsbibliothek Hamburg user
on 19 December 2017

Gal, M., Reading, A.M., Ellingsen, S., Koper, K.D., Burlacu, R. & Gibbons, S.J., 2016. Deconvolution enhanced direction of arrival estimation using one- and three-component seismic arrays applied to ocean induced microseisms, *Geophys. J. Int.,* **206**(1), 345–359.

Gregersen, S., 1978. Possible mode conversion between Love and Rayleigh waves at a continental margin, *Geophys. J. R. astr. Soc.,* **54,** 121–127.

Grevemeyer, I., Herber, R. & Essen, H.-H., 2000. Microseismological evidence for a changing wave climate in the northeast Atlantic ocean, *Nature,* **408**(6810), 349–352.

Gualtieri, L., Stutzmann, E., Capdeville, Y., Ardhuin, F., Schimmel, M., Mangeney, A. & Morelli, A., 2013. Modelling secondary microseismic noise by normal mode summation, *Geophys. J. Int.,* **193**(3), 1732–1745.

Hasselmann, K., 1963. A statistical analysis of the generation of microseisms, *Rev. Geophys.,* **1**(2), 177–210.

Haubrich, R.A. & McCamy, K., 1969. Microseisms: Coastal and pelagic sources, *Rev. Geophys.,* **7**(3), 539–571.

Jobert, N. & Jobert, G., 1983. An application of ray theory to the propagation of waves along a laterally heterogeneous spherical surface, *Geophys. Res. Lett.,* **10**(12), 1148–1151.

Juretzek, C. & Hadziioannou, C., 2016. Where do ocean microseisms come from? A study of Love-to-Rayleigh wave ratios, *J. geophys. Res.,* **121**(9), 6741–6756.

Kendall, M.G., 1938. A new measure of rank correlation, *Biometrika,* **30**(1/2), 81–93.

Kennett, B.L.N., 1972. Seismic wave scattering by obstacles on interfaces, *Geophys. J. R. astr. Soc.,* **28**(3), 249–266.

Kennett, B.L.N. & Mykkeltveit, S., 1984. Guided wave propagation in laterally varying media—II. Lg-waves in north-western Europe, *Geophys. J. R. astr. Soc.,* **79**(1), 257–267.

Kimman, W., Campman, X. & Trampert, J., 2012. Characteristics of seismic noise: fundamental and higher mode energy observed in the northeast of the Netherlands, *Bull. seism. Soc. Am.,* **102**(4), 1388–1399.

Kozlovskaya, E., 2007. Seismic network XK:LAPNET/POLENET seismic temporary array (RESIF-SISMOB), RESIF – Réseau Sismologique et géodeéique Français, https://doi.org/10.15778/resif.xk2007.

Lin, F.-C., Moschetti, M.P. & Ritzwoller, M.H., 2008. Surface wave tomography of the western United States from ambient seismic noise: Rayleigh and Love wave phase velocity maps, *Geophys. J. Int.,* **173,** 281–298.

Matsuzawa, T., Obara, K., Maeda, T., Asano, Y. & Saito, T., 2012. Love- and Rayleigh-wave microseisms excited by migrating ocean swells in the North Atlantic detected in Japan and Germany, *Bull. seism. Soc. Am.,* **102**(4), 1864–1871.

McGarr, A., 1969. Amplitude variations of Rayleigh waves – propagation across a continental margin, *Bull. seism. Soc. Am.,* **59**(3), 1281–1305.

Möllhoff, M. & Bean, C.J., 2016. Seismic noise characterization in proximity to strong microseism sources in the Northeast Atlantic, *Bull. seism. Soc. Am.,* **106**(2), 464–477.

Nishida, K., Kawakatsu, H., Fukao, Y. & Obara, K., 2008. Background Love and Rayleigh waves simultaneously generated at the Pacific Ocean floors, *Geophys. Res. Lett.,* **35,** L16307, doi:10.1029/2008GL034753.

Oliver, J., 1962. A summary of observed seismic surface wave dispersion, *Bull. seism. Soc. Am.,* **52**(1), 81–86.

Paulssen, H., Levshin, A.L., Lander, A.V. & Snieder, R., 1990. Time- and frequency-dependent polarization analysis: anomalous surface wave observations in Iberia, *Geophys. J. Int.,* **103**(2), 483–496.

Poli, P., Pedersen, H., Campillo, M. & the POLENET/LAPNET Working Group, 2013. Noise directivity and group velocity tomography in a region with small velocity contrasts: the northern Baltic shield, *Geophys. J. Int.,* **192**(1), 413–424.

Riahi, N., Bokelmann, G., Sala, P. & Saenger, E.H., 2013. Time-lapse analysis of ambient surface wave anisotropy: a three-component array study above an underground gas storage, *J. geophys. Res.,* **118**(10), 5339–5351.

Sadeghisorkhani, H., Gudmundsson, Ó., Roberts, R. & Tryggvason, A., 2016. Mapping the source distribution of microseisms using noise covariogram envelopes, *Geophys. J. Int.,* **205**(3), 1473–1491.

Saito, T., 2010. Love-wave excitation due to the interaction between a propagating ocean wave and the sea-bottom topography, *Geophys. J. Int.,* **182**(3), 1515–1523.

Schimmel, M., Stutzmann, E., Ardhuin, F. & Gallart, J., 2011. Polarized Earth's ambient microseismic noise, *Geochem. Geophys. Geosyst.,* **12,** Q07014, doi:10.1029/2011GC003661.

Stutzmann, E., Schimmel, M., Patau, G. & Maggi, A., 2009. Global climate imprint on seismic noise, *Geochem. Geophys. Geosyst.,* **10,** Q11004, doi:10.1029/2009GC002619.

The ObsPy Development Team, 2016. *August 3. Obspy 1.0.2*. Zenodo, http://doi.org/10.5281/zenodo.49636.

Tolman, H.L., 1991. A third-generation model for wind waves on slowly varying, unsteady, and inhomogeneous depths and currents, *J. phys. Oceanogr.,* **21**(6), 782–797.

van Driel, M., Krischer, L., Stähler, S.C., Hosseini, K. & Nissen-Meyer, T., 2015. Instaseis: instant global seismograms based on a broadband waveform database, *Solid Earth Discuss.,* **7,** 957–1005.

Wathelet, M., 2008. An improved neighborhood algorithm: parameter conditions and dynamic scaling, *Geophys. Res. Lett.,* **35,** L09301, doi:10.1029/2008GL033256.

Yang, Y. & Ritzwoller, M.H., 2008. Characteristics of ambient seismic noise as a source for surface wave tomography, *Geochem. Geophys. Geosyst.,* **9,** Q02008, doi:10.1029/2007GC001814.

Young, A.P., Guza, R.T., Adams, P.N., O'Reilly, W.C. & Flick, R.E., 2012. Cross-shore decay of cliff top ground motions driven by local ocean swell and infragravity waves, *J. geophys. Res.,* **117,** C06029, doi:10.1029/2012JC007908.

Young, A.P., Guza, R.T., Dickson, M.E., O'Reilly, W.C. & Flick, R.E., 2013. Ground motions on rocky, cliffed, and sandy shorelines generated by ocean waves, *J. geophys. Res.,* **118**(12), 6590–6602.

SUPPORTING INFORMATION

Supplementary data are available at *GJIRAS* online.

Table S1. Regional earthquakes used for great circle path deviation estimates.

Figure 1. Sequence of ocean surface elevation PSD (colour range) from February 24 and 25, 2009 and array based localization of noise sources for transversal (a) and vertical (b) beamforming results at a period of 14 s (black crosses: more than 75 per cent of maximum beampower; red cross: beampower maximum). Time labels indicate averaging period for beamform results.

Please note: Oxford University Press is not responsible for the content or functionality of any supporting materials supplied by the authors. Any queries (other than missing material) should be directed to the corresponding author for the paper.

Downloaded from https://academic.oup.com/gji/article-abstract/211/3/1640/4209579
by Staats- und Universitätsbibliothek Hamburg user
on 19 December 2017